nature physics

ARTICLES

https://doi.org/10.1038/s41567-018-0268-8

3D field phase-space control in tokamak plasmas

Jong-Kyu Park[1*], YoungMu Jeon[2], Yongkyoon In[2], Joon-Wook Ahn[3], Raffi Nazikian[1], Gunyoung Park[2], Jaehyun Kim[2], HyungHo Lee[2], WonHa Ko[2], Hyun-Seok Kim[2], Nikolas C. Logan[1], Zhirui Wang[1], Eliot A. Feibush[1], Jonathan E. Menard[1] and Michael C. Zarnstroff[1]

A small relaxation of the axisymmetric magnetic field of a tokamak into a non-axisymmetric three-dimensional (3D) configuration can be effective to control magnetohydrodynamic instabilities, such as edge-localized modes. However, a major challenge to the concept of 3D tokamaks is that there are virtually unlimited possible choices for a 3D magnetic field, and most of them will only destabilize or degrade plasmas by symmetry breaking. Here, we demonstrate the phase-space visualization of the full 3D field-operating windows of a tokamak, which allows us to predict which configurations will maintain high confinement without magnetohydrodynamic instabilities in an entire region of plasmas. We test our approach at the Korean Superconducting Tokamak Advanced Research (KSTAR) facility, whose 3D coils with many degrees of freedom in the coil space make it unique for this purpose. Our experiments show that only a small subset of coil configurations can accomplish edge-localized mode suppression without terminating the discharge with core magnetohydrodynamic instabilities, as predicted by the perturbative 3D expansion of plasma equilibrium and the optimizing principle of local resonance. The prediction provided excellent guidance, implying that our method can substantially improve the efficiency and fidelity of the 3D optimization process in tokamaks.

Massive fusion burning plasmas will be tested first in a tokamak, a toroidally axisymmetric device for magnetic confinement, as planned in the International Tokamak Experimental Reactor (ITER)[1]. It is the symmetry in magnetic field $\mathbf{B}_0$ that enables a tokamak to sustain hot plasmas more efficiently than other confinement concepts, and thus any unexpected departure from the symmetry must be prohibited, which is commonly called error field (EF) control[2–5]. The strict requirement for axisymmetry, however, also means limited access to magnetic field spectra, and consequently to the control of fundamental transport and instabilities. Indeed, great utility of non-axisymmetric three-dimensional (3D) fields $\delta\mathbf{B}$ has been discovered in tokamak operation, as has been highlighted by edge-localized mode (ELM) control using a resonant magnetic perturbation (RMP)[6–14]. As discussed in the literature, ELM crashes are repetitive energy losses when the self-organized pressure gradient in the edge pedestal, ∇p_{ped}, becomes steep enough to trigger local magnetohydrodynamic (MHD) peeling–ballooning instabilities[15–17]. These ELMs can cause unrepairable damage to plasma-facing components and thus must be controlled in a reactor-scale tokamak[18]. RMP is an outstanding tool to entirely suppress ELMs by externally controllable means while potentially providing transport required for ash removal and impurity exhaust[19,20].

RMP ELM suppression and EF control encapsulate the two opposing sides of non-axisymmetry in a tokamak. It is necessary to relax the symmetry slightly to a 3D state in order to ease the control of transport and instabilities, but the relaxation must not be accompanied by a major degradation in the core confinement or a disruptive MHD instability. It is a major challenge for tokamak science to optimize and use 3D magnetic fields so that their consequence remains only beneficial. Furthermore, the number of choices available in 3D space is virtually unlimited, leaving no alternative other than a predictive optimization. In this article, we demonstrate the phase-space visualization of the full 3D field-operating windows in a tokamak, to maintain high confinement without MHD instabilities from the core to the edge of plasmas.

The first key to optimizing 3D fields in a tokamak is to understand and control a special class of 3D fields called resonant magnetic perturbation. RMP resonates with the plasma through rational magnetic surfaces, where magnetic field lines close in on themselves after m toroidal transits and n poloidal transits. A rational surface at the so-called safety factor $q=m/n$ becomes fragile to the RMP of the same pattern, that is, $\mathcal{J}(\delta\mathbf{B}\cdot\nabla\psi)\propto\Phi_{mn}(\psi)\mathrm{e}^{\mathrm{i}(m\vartheta-n\varphi)}$, with the label of magnetic surfaces ψ, the poloidal angle ϑ, the toroidal angle φ and volume-element Jacobian $\mathcal{J}$. As implied by the Kolmogorov–Moser–Arnold theorem[21–23] on the field line Hamiltonian system, a RMP can form magnetic islands and/or stochastic field lines, while a non-resonant magnetic perturbation (NRMP) maintains magnetic surfaces. A NRMP can modify fundamental transport across magnetic surfaces to be non-ambipolar[24] and can eventually become important, but should be considered as the next order.

Impact of resonant 3D fields

The powerful impact of RMPs on tokamak control is well illustrated in Fig. 1, which shows a unprecedentedly long MHD-free operation of high-confinement mode (H-mode) by an $n=1$ RMP in the Korean superconducting tokamak advanced research (KSTAR)[25] facility. This is a typical H-mode discharge in KSTAR with plasma current $I_{\mathrm{P}}=0.52$ MA, toroidal field $B_{\mathrm{T}}=1.8$ T, $q_{95}=5.0$–5.2 at the surface in the edge where the normalized poloidal flux is up to 95%, that is, $\psi_{\mathrm{N}}=0.95$, and with shaping parameters such as elongation $\kappa\sim1.8$ and mean triangularity $\delta\sim0.56$. The spikes in D_α emission measured in the lower divertor in Fig. 1a correspond to the hard sputtering of main deuterium ions due to type-I ELM[15] crashes. The intensity of the crashes is strongly mitigated as soon as the RMP is applied, and finally suppressed after initial relaxation. Figure 1b shows the line-integrated electron density $n_{\mathrm{e}}>2.1\times10^{19}\,\mathrm{m}^{-3}$, core electron temperature $T_{\mathrm{e}}>3.3$ keV, ion temperature $T_{\mathrm{i}}>3.7$ keV, maintained

[1]Princeton Plasma Physics Laboratory, Princeton, NJ, USA. [2]National Fusion Research Institute, Daejeon, South Korea. [3]Oak Ridge National Laboratory, Oak Ridge, TN, USA. *e-mail: jpark@pppl.gov

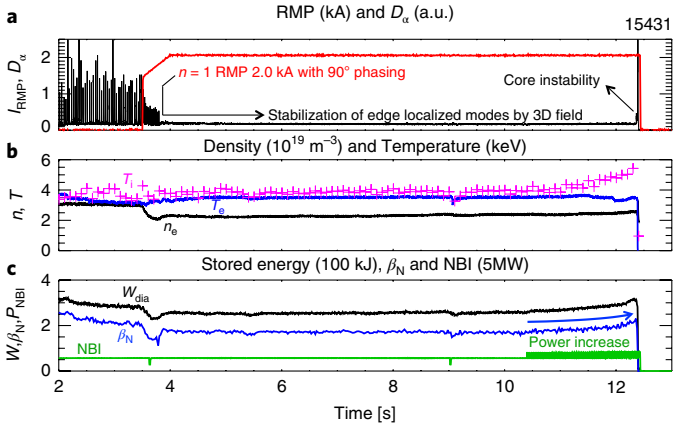

Fig. 1 | MHD-stable tokamak operation with 3D fields. a, D_α emission (black) showing ELM crashes and suppression by $n=1$ RMP (red). **b**, n_e measured by interferometer, T_e inferred from electron cyclotron emission, and T_i inferred from two-Gaussian fitting[44] for charge-exchange background emission by carbon impurities. **c**, W measured by a diamagnetic loop, β_N and NBI power.

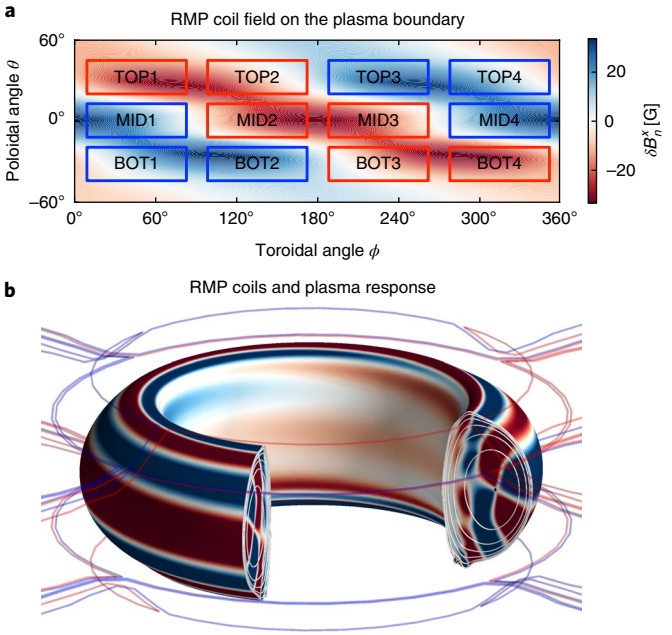

Fig. 2 | KSTAR 3D coils and fields. a, The plane projection. **b**, The actual geometry. The colour corresponds to the current in the coils in the standard 90° $n=1$ configuration, with red designating positive and blue representing negative current. The contour underneath in **a** shows externally applied 3D fields on the plasma boundary, and the 3D contour in **b** shows 3D fields on perturbed flux surfaces due to plasma response. The modelled resonant surfaces are indicated by white solid lines.

throughout ELM suppression. The stored energy $W>0.25$ MJ is also shown in Fig. 1c, with a normalized ratio of thermal to magnetic pressure[26] $\beta_N=1.7$–2.0 T m MA^{-1}, produced by the neutral beam injection (NBI) heating power of approximately 3 MW. One can see that the RMP causes n_e density pumping and thus a degradation of energy confinement, up to $\Delta H_{89}\sim12\%$ and $\Delta H_{98}\sim25\%$ in terms of the so-called H-factors[1], in this particular case. A small loss of confinement is inevitable in a symmetry-breaking field application, but can be minimized by optimizing RMP currents near the threshold of ELM suppression. The disruption at the end of this discharge is attributed to a deliberate NBI power increment and the subsequent locked mode (LM) instability[2], as will be revisited later. The resulting disruption highlights the importance of the remnant core EF control in the applications of RMP.

The RMP in this example has been extensively tested on hundreds of different KSTAR discharges, but it is just one of many RMPs that can be produced by the coils shown in Fig. 2. The three rows of internal coils, at the top, middle and bottom, are unique in KSTAR, giving greater flexibility for spectrum control than other existing large tokamaks but also making it almost impossible to test all spectral variations in numerous discharge conditions.

Plasma response to 3D fields

In order to predict the functionality of each RMP, one must understand coupling between the externally applied field $\mathbf{\Phi}^x$ from 3D coils and the resonant field Φ_{mn} established at the rational surfaces. For the purpose of stable ELM control, the RMP must be strong enough to modify the profiles in the edge, but not the core. This core–edge RMP decoupling, as well as the total RMP strength, are the two obvious optimizing principles for ELM control, although they were mostly implicit in past studies due to limited accessibility to the RMP spectrum.

The prediction of $\Phi_{mn}[\mathbf{\Phi}^x]$ has involved various physics models[27–35], but none is yet universally successful. The plasma equilibrium must be close to a Maxwellian and thus evolves to $\delta\mathbf{j}\times\mathbf{B}_0+\mathbf{j}_0\times\delta\mathbf{B}=\nabla\delta p$ with a small 3D field $|\delta\mathbf{B}|/|\mathbf{B}_0|=10^{-3}$–$10^{-4}$ in Alfvén τ_A to sound wave damping τ_s time scales. This ideal evolution does not allow a topological change of magnetic field, requiring localized parallel currents $(\delta j_{||}/B_0)_{mn}$ to screen Φ_{mn} at the resonant layer. In the slower time scales, the plasma can evolve non-ideally due to the dynamics in the neighbourhood of resonant layers. The narrowness of the layers allows the use of boundary layer theory through the asymptotic matching from each resonant surface to the outer-layer Δ_{mn}, which represents the jump in $[\partial(\mathcal{J}(\delta\mathbf{B}\cdot\nabla\psi))_{mn}/\partial\psi]^+$ across the layer due to $\delta\mathbf{j}_{||}$. Ampere's law $\mu_0\delta\mathbf{j}_{||}=\nabla\times\delta\mathbf{B}$, with the permeability of free space μ_0, then renders the resonant field Φ_{mn}, which is a convenient measure for the initial boundary conditions exerted by RMP that can later drive the layer evolution.

The separation of the outer and inner regions of the resonant layers is central in a reduced 3D tokamak model. $(\Phi_{mn})_o$ in the outer region is ruled by ideal MHD but must be globally consistent with complicated 3D coils. $(\Phi_{mn})_i$ in the inner region is driven by non-ideal physics although it is localized. Asymptotic matching between $(\Phi_{mn})_o$ and $(\Phi_{mn})_i$ allows unified physics descriptions of the two regions of different complexities. In particular, $(\Phi_{mn})_o=(\Phi_{mn})_{crit}$ at the onset of the bifurcation. This "field penetration" process is well known to cause LMs in the core[29], but also assumed here to suppress ELMs when it is localized in the edge. This supposition differs from the popular "vacuum island overlap width" method[6–12], which essentially approximates $(\Phi_{mn})_o$ by the vacuum resonant field Φ^x_{mn}. The misleading nature of this approximation is not easily seen unless 3D EFs are strongly involved[4,5] or 3D coils are flexible enough to de-correlate $(\Phi_{mn})_o$ from Φ^x_{mn}[13,34].

3D field phase space and operating windows

The RMP optimizing principles can then be quantitatively expressed by the two conditions, $\Phi_E(\mathbf{I})\geq(\Phi_E)_{crit}$ and $\Phi_C(\mathbf{I})<(\Phi_C)_{crit}$, to suppress edge MHD instabilities while avoiding disruptive core field penetration. Here, $\Phi_{C,E}\equiv\left(\sum|\Phi_{mn}|^2_o/N\right)^{1/2}$ represent the core and edge RMP strength respectively, and each of N rational surfaces must be properly chosen depending on 3D perturbed equilibria (see Methods). The 3D coil phase space, $\mathbf{I}$, is six dimensional for $n=1$ in KSTAR, as each top/middle/bottom row of coils can generate an $n=1$ field with an arbitrary toroidal phase ϕ, that is, $\mathbf{I}=(I_T,I_M,I_B,\phi_T,\phi_M,\phi_B)$. Note that an axisymmetric plasma

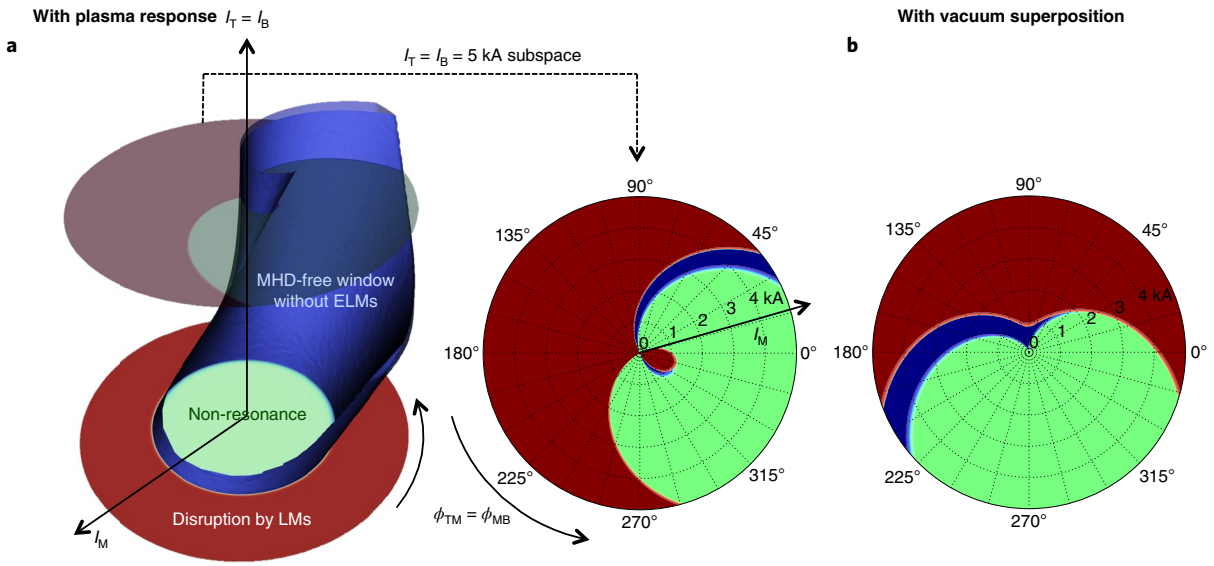

Fig. 3 | Stable 3D field-operating window in the $n=1$ coil phase space. a,**b**, MHD-free blue window in the 3D coil phase space (I, I_M, ϕ) and in the 2D subset ($I=5$ kA, I_M, ϕ) predicted by ideal response modelling (**a**) and the same 2D subset based on vacuum modelling (**b**). The red region is where the LM-driven disruption is predicted, and the green zone is where weak resonant response is predicted.

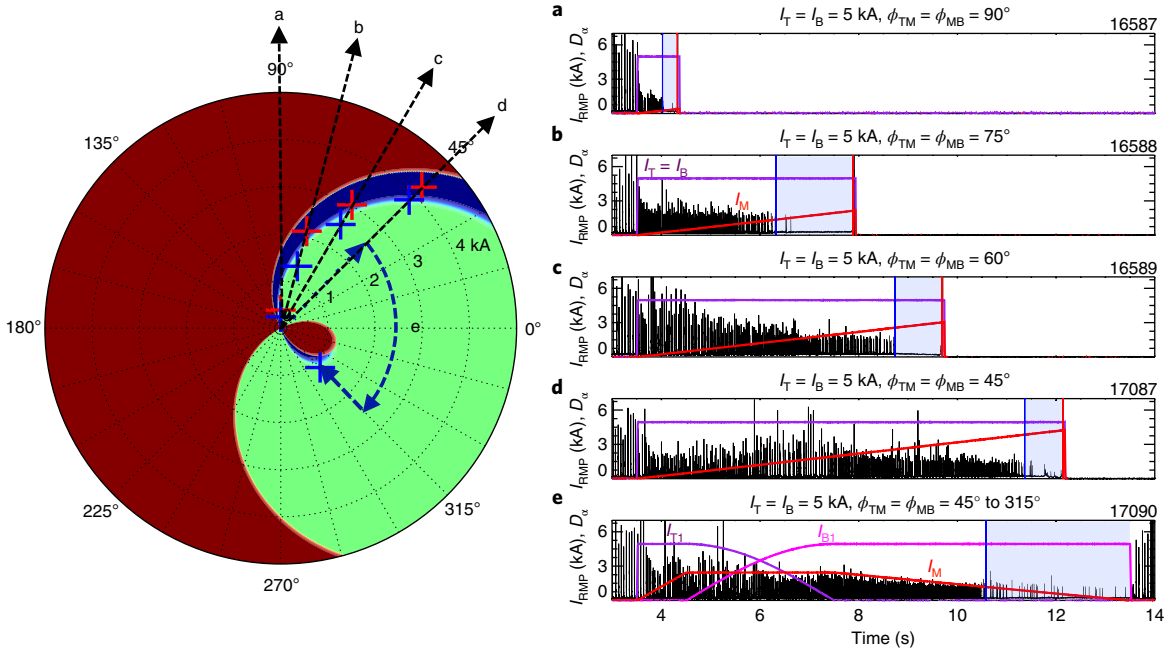

Fig. 4 | Validation of predicted 3D field-operating window. Right, **a**–**d**, The I_M coil current was ramped up with fixed $I=I_T=I_B$ and $\phi=\phi_{TM}=\phi_{MB}$. **e**, I_M and ϕ were varied dynamically to take the path in the stability domain shown on the left. The vertical lines on the right indicate the times of the thresholds for ELM suppression (blue) and LM disruption (red), which are indicated on the left by plus signs. The blue shadow between the vertical lines corresponds to each MHD-free window, as can be seen by suppressed D_α spikes. The agreement between experiments and predictions is remarkable, given the localized narrow windows in the large phase space. This result is also briefly introduced in a Fusion Energy Conference paper that summarizes 3D physics studies in the 2016 KSTAR experimental campaign[45].

responds identically to the RMP independent of reference toroidal phase unless there is an intrinsic non-axisymmetry, which is negligible in KSTAR[36]. This reduces the number of variables to five, (I_T, I_M, I_B, ϕ_{TM}, ϕ_{MB}), where $\phi_{TM}=\phi_T-\phi_M$ and $\phi_{MB}=\phi_M-\phi_B$ and further down to three, (I, I_M, ϕ), where $I\equiv I_T=I_B$ and $\phi\equiv\phi_{TM}=\phi_{MB}$, considering only the up–down symmetric cases.

This study adopted the ideal perturbed equilibrium code (IPEC)[37] to evaluate $\Phi_{C,E}(\mathbf{I})$ in the entire coil phase space available for KSTAR, and the critical RMP values $(\Phi_{C,E})_{crit}$ at one empirical operating point as implied from a number of standard RMP ($I=I_M$,$\phi=90°$) experiments (discussed further in Methods). Specifically, $\Phi_E(I, I_M, \phi) \geq \Phi_E(I=I_M=1.8\,\text{kA}, \phi=90°)$ and $\Phi_C(I, I_M, \phi) < \Phi_C(I=I_M=2.1\,\text{kA}, \phi=90°)$ for the two RMP optimizing conditions, giving the blue MHD-free operating window in Fig. 3. The window is complicated even in this reduced coil space, and occupies only a small fraction of phase-space volume, manifesting the

difficulties in finding RMP windows without model guidance. An important supposition here is that the $(\Phi_{C,E})_{crit}$ evaluated by the proposed method is independent of **I**, or any variation of 3D fields, since the outer-layer model is sufficiently accurate and can be isolated from the inner-layer dynamics. The ability to make these single-point perspective mappings to the entire 3D field phase space is also critical to validate any outstanding layer models for $(\Phi_{C,E})_{crit}$[29,38] across different regimes and devices.

Validation of 3D field-operating windows

A set of KSTAR experiments that will be introduced here was carefully designed to test the predicted window. In particular, an interesting subset of the coil configuration was selected, ($I=5$ kA, I_M, ϕ), as shown in Fig. 3a. In this subset, the prediction becomes clearly contrasted to the vacuum prediction shown in Fig. 3b. The favourable toroidal phasing ϕ for ELM suppression is almost opposite to the vacuum prediction, and the isolated blue window in Fig. 3a near the centre of the diagram does not exist in Fig. 3b. Note that recent $n=2$ RMP experiments in DIII-D using two rows of internal coils were also successful in differentiating the two model predictions[34], but here the difference is greatly amplified by the addition of the third row.

The experimental results demonstrated remarkable predictability of ELM suppression windows using the proposed method. Figure 4a–d shows each experiment with a coil current I_M ramp, while fixing $I=5$ kA, in each different phasing $\phi=90°$, 75°, 60°, 45° where the existence of an MHD-free window is predicted. In each case, ELMs were strongly mitigated and then suppressed, and the ELM suppression lasted until the coil currents become large enough to cause LM disruption.

On the left in Fig. 4, the measured ELM suppression thresholds (blue plus signs) as well as LM disruption thresholds (red plus signs) are overlaid in the phase space to compare with the prediction. The most interesting test is shown Fig. 4e, which explored the isolated MHD-free window near the centre of the diagram. In order to safely hit the window without passing through the red zone due to LMs, the coil current waveforms are designed to take the dynamic path (e) as illustrated on the phase-space diagram. It is somewhat counter-intuitive to see the ELM suppression during the I_M ramp-down phase, but this is a consequence of the increased Φ_E that was cancelled between I and I_M. This dynamic path can only be devised by developing a road map based on the visualized MHD-free path on the phase space.

Resonant field amplification effects

The predicted RMP operating windows can significantly vary when the 3D plasma response changes, for example due to the resonant field amplification (RFA) driven by the least stable kink mode[39]. Figure 5a shows a phase-space plot in (I, β_N), where $I=I_M$,$\phi=90°$ in the standard RMP operation, as predicted by IPEC modelling using equilibria with different pressure p and thus β_N. In higher β_N, the currents required to reach the ELM suppression window are smaller due to the RFA, but the window becomes narrower since Φ_C increases faster than Φ_E. This explains the LM-driven disruption at the end of discharge no. 15431 in Fig. 1 reasonably well, as indicated in Fig. 5a.

The RFA also provides the explanation for the sporadic ELMs observed during the ELM-suppressing phase in Fig. 4e. The major variations of ELM peaks seen in $D_\alpha(t)$ in Fig. 5b are due to the dynamically changed RMP, but the small transient oscillations for $t>10$ s are due to the time-varying β_N, as can be seen in $\Phi_E(t)$ simulated with the scaled RFA.

It is also interesting to see that a modelled toroidal torque based on collisionless drift-kinetic MHD is well correlated with the core rotation evolution, as shown in Fig. 5c. This torque, often called neoclassical toroidal viscosity (NTV)[24,40], is another hidden

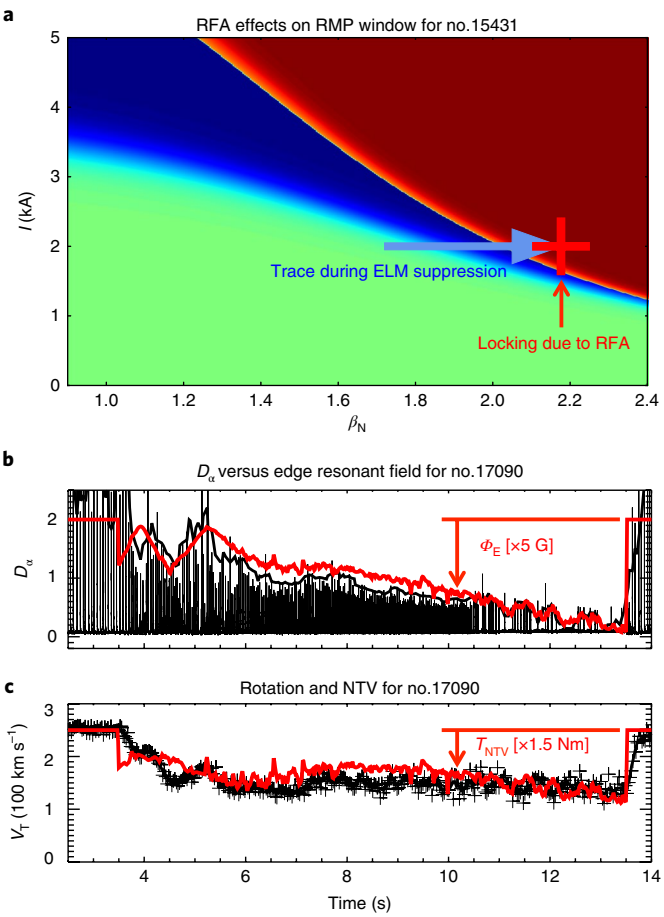

Fig. 5 | Plasma amplification and response to 3D fields. a, Predicted MHD-free window (blue) as a function of β_N for standard RMP with ($I=I_M$, $\phi=90°$), showing the RFA and explaining the LM instability in discharge no. 15431 (Fig. 1). **b**,**c**, Evolution of RMP and NRMP coupling predicted in the dynamic path (Fig. 4e); the comparison between Φ_E and ELM peaks with five-point box averaged envelope (**b**); the correlation between NTV torque and rotation (**c**).

functionality of 3D fields. The ability to predict the NTV effects is important to estimate $\Phi_{C,E}$ more precisely in high-β_N plasmas. The ideal simulation used in this study tends to overestimate the RFA when approaching to the no-wall stability limit[41], where 3D response should be self-consistent with the strong drift-kinetic effects[42,43].

Extended 3D field-operating windows

Phase-space visualization can also provide an important guidance to the design and optimization of new 3D coils. Note that this study is not to promote the $n=1$ RMP scenario for ITER or future reactors. In fact, the narrowness of the MHD-free window is a consequence of strong $n=1$ coupling to the core, which can be alleviated if higher-n RMPs are used. Although the present KSTAR 3D coils have only four toroidal sectors for each row, one can test the optimizing principles for $n=2$ by assuming a future upgrade to eight toroidal sectors and evaluating the $n=2$ $\Phi_{C,E}$. A new $(\Phi_{C,E})_{crit}$ is also required and again empirically determined. The threshold is taken from the 2016 discharge no. 16574, where the ELM suppression was transiently obtained when $q_{95}\sim3.8$ at $t=5.85$ s and later locked when $q_{95}\sim3.5$ at $t=6.5$ s (also see Methods). The information captured in this single discharge allows visualization of the entire $n=2$ MHD-stable windows in the coil space, with $\Phi_E(I, I_M, \phi)\geq\Phi_E(I=I_M=3\,\text{kA}, \phi=90°, t=5.85\,\text{s})$ and $\Phi_C(I, I_M, \phi)\leq\Phi_C(I=I_M=3\,\text{kA}, \phi=90°, t=6.5\,\text{s})$, which can be tested in experiments.

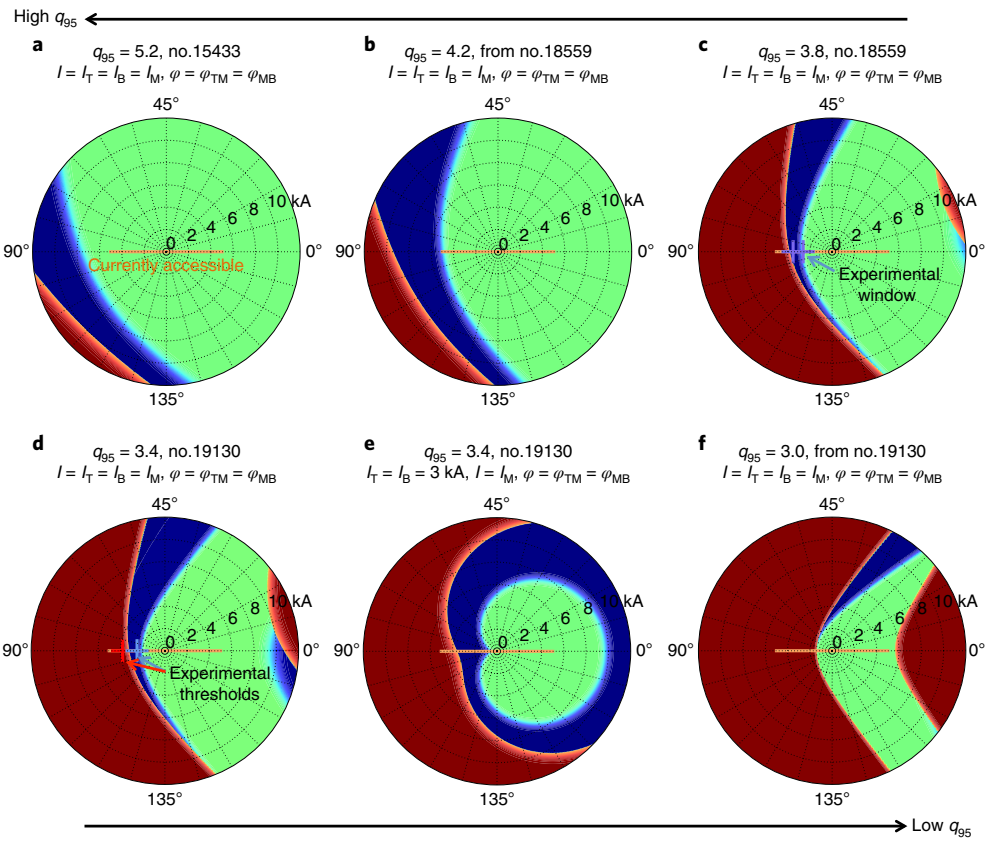

Fig. 6 | Stable 3D field-operating windows in the $n = 2$ coil phase space. a, For the same target as used for $n = 1$, illustrating a wider window in principle but higher currents required to hit the threshold beyond the practical limit 5 kA. **b**,**f**, When q_{95} decreases, the ELM suppression window becomes accessible marginally when $q_{95} < 4.2$ (**b**) but disappears when $q_{95} \sim 3.0$ (**f**), as consistent with the experimental q window $q_{95} = 3.3$–4.1. **c**,**d**, Cases where the stable ELM suppression was obtained as indicated. **a**–**f**, The ELM suppression window can be enlarged in the space where KSTAR can currently access (**e**), but the optimal RMP operating point is located generally between $\phi = 0°$ and $\phi = 90°$.

While $n = 2$ ELM suppression was only marginal in the 2016 target plasmas, it became more stable in the 2017 target plasmas with higher triangularity and up–down asymmetry. Still, the $n = 2$ was not as reliable as $n = 1$ for ELM suppression, and the phase-space visualization in Fig. 6 explains why. Note that the phase-space plot is extended to 10 kA for $0° \leq \phi \leq 180°$, although the present KSTAR coils can access only 5 kA with $\phi = 0°$, 90°, as shown in each diagram. In the highest $q_{95} = 5.2$ case (Fig. 6a), which is the same target as studied for $n = 1$, the ELM suppression window is wider than for $n = 1$ but reachable only with currents higher than 5 kA. This reflects the advantage for RMP decoupling but also the disadvantage for RMP strength for higher n, due to the faster radial attenuation. When q_{95} decreases, the ELM suppression window becomes accessible marginally when $q_{95} < 4.2$ (Fig. 6b) but disappears when $q_{95} \sim 3.0$ (Fig. 6f) due to the strong core coupling. As is indeed consistent with this prediction, successful $n = 2$ ELM suppression in KSTAR over the years has been found only for $q_{95} = 3.3$–4.1. Figure 6c,d shows the experimentally observed ELM suppression windows, although discharge no. 18559 tested only $I < 3.5$ kA where no locking was observed. Clearly, the currently available phasing is not optimal, and much wider windows exist between $\phi = 0°$ and 90°. There is still room for improvement even with the fixed $\phi = 0°$ or 90°, by selecting a different coil subset as illustrated in Fig. 6e. In general, however, new capability to rotate the $n = 2$ toroidal phase would be beneficial for KSTAR to achieve more reliable ELM suppression.

Outlook

The proposed method with $\Phi_{C,E}(\mathbf{I})$ here can be applied for ITER, where currently three rows of in-vessel coils are considered for ELM control in addition to three rows of ex-vessel coils for EF control. Depending on the n, the phase-space dimensionality of 3D coils in ITER can be elevated to 12. The free optimization of 3D coils is another important application, as the dimension of $\mathbf{I}$ becomes as large as the number of (m, n) retained on a control surface where a 3D field can be uniquely specified. The investigation of innovative 3D coils is critical for a fusion reactor beyond ITER, since in-vessel coils are undesirable in a radioactive environment. The prediction of $(\Phi_{C,E})_{crit}$ in ITER or reactor regimes is also necessary, but sufficient just at one operating point in the phase space of 3D coils and main equilibrium parameters, as demonstrated throughout this article.

RMP is dominant in 3D fields but not the full story in 3D field optimization. A NRMP can change toroidal momentum transport, and eventually $(\Phi_{C,E})_{crit}$ and other plasma instabilities. This NRMP effect occurs non-linearly to the strength and spectrum of 3D fields, but still can be simplified and described by a single matrix function using a self-consistent determination between response and transport[43]. This more general perturbed equilibrium code approach essentially turns the complicated 3D tokamak optimization into a simple matrix exercise, with RMP and NRMP coupling matrices for given 2D profiles, providing first-order answers efficiently for complicated 3D tokamak physics problems.

Methods

Methods, including statements of data availability and any associated accession codes and references, are available at https://doi.org/10.1038/s41567-018-0268-8.

Received: 31 July 2017; Accepted: 27 July 2018;
Published online: 10 September 2018

References

1. Ikeda, K. Progress in the ITER physics basis. *Nucl. Fusion* **47**, S1–S17 (2007).
2. Fitzpatrick, R. & Hender, T. C. The Interaction of resonant magnetic perturbations with rotating plasmas. *Phys. Fluids B* **3**, 644–673 (1991).
3. Buttery, R. J. et al. Error field mode studies on JET, COMPASS-D and DIII-D, and implications for ITER. *Nucl. Fusion* **39**, 1827–1835 (1999).
4. Park, J.-K., Schaffer, M. J., Menard, J. E. & Boozer, A. H. Control of asymmetric magnetic perturbations in tokamaks. *Phys. Rev. Lett.* **99**, 195003 (2007).
5. Paz-Soldan, C. et al. The importance of matched poloidal spectra to error field correction in DIII-D. *Phys. Plasmas* **21**, 072503 (2014).
6. Evans, T. E. et al. Suppression of large edge-localized modes in high-confinement DIII-D plasmas with a stochastic magnetic boundary. *Phys. Rev. Lett.* **92**, 235003 (2004).
7. Evans, T. E. et al. Edge stability and transport control with resonant magnetic perturbations in collisionless tokamak plasmas. *Nat. Phys.* **2**, 419–423 (2006).
8. Evans, T. E. et al. RMP ELM suppression in DIII-D plasmas with ITER similar shapes and collisionalities. *Nucl. Fusion* **48**, 024002 (2008).
9. Liang, Y. et al. Active control of type-I edge-localized modes with $n=1$ perturbation fields in the JET tokamak. *Phys. Rev. Lett.* **98**, 265004 (2007).
10. Suttrop, W. et al. First observation of edge localized modes mitigation with resonant and nonresonant magnetic perturbations in ASDEX Upgrade. *Phys. Rev. Lett.* **106**, 225004 (2011).
11. Kirk, A. et al. Observation of lobes near the X point in resonant magnetic perturbation experiments in MAST. *Phys. Rev. Lett.* **108**, 255003 (2012).
12. Jeon, Y. M. et al. Suppression of edge localized modes in high-confinement KSTAR plasmas by nonaxisymmetric magnetic perturbations. *Phys. Rev. Lett.* **109**, 035004 (2012).
13. Nazikian, R. et al. Pedestal bifurcation and resonant field penetration at the threshold of edge-localized mode suppression in the DIII-D tokamak. *Phys. Rev. Lett.* **114**, 105002 (2015).
14. Sun, Y. et al. Nonlinear transition from mitigation and suppression of the edge localized mode with resonant magnetic perturbations in the EAST tokamak. *Phys. Rev. Lett.* **117**, 115001 (2016).
15. Zohm, H. Edge localized modes (ELMs). *Plasma Phys. Control. Fusion* **38**, 105–128 (1996).
16. Connor, J. W. A review of models for ELMs. *Plasma Phys. Control. Fusion* **40**, 191–213 (1998).
17. Snyder, P. et al. Stability and dynamics of the edge pedestal in the low collisionality regime: physics mechanisms for steady-state ELM-free operation. *Nucl. Fusion* **47**, 961–968 (2007).
18. Hawryluk, R. et al. Principal physics developments evaluated in the ITER design review. *Nucl. Fusion* **49**, 065012 (2009).
19. Loarte, A. et al. Progress on the application of ELM control schemes to ITER scenarios from the non-active phase to DT operation. *Nucl. Fusion* **54**, 033007 (2014).
20. Schmitz, O. et al. Enhancement of helium exhaust by resonant magnetic perturbation fields at LHD and TEXTOR. *Nucl. Fusion* **56**, 106011 (2016).
21. Kolmogorov, A. N. On the preservation of conditionally periodic motions under small variations of the Hamilton function. *Dokl. Akad. Nauk SSSR* **98**, 527–530 (1954).
22. Arnol'd, V. I. Small denominators and problems of stability of motion in classical and celestial mechanics. *Russ. Math. Surveys* **18**, 85–191 (1963).
23. Möser, J. On invariant curves of area-preserving mappings of an annulus. *Machr. Akad. Wiss. Goett. II, Math.-Phys. Kl.* **2a**, 1–20 (1962).
24. Park, J.-K., Boozer, A. H. & Menard, J. E. Nonambipolar transport by trapped particles in tokamaks. *Phys. Rev. Lett.* **102**, 065002 (2009).
25. Lee, G. S. et al. The KSTAR Project: An advanced steady state superconducting tokamak experiment. *Nucl. Fusion* **40**, 575–582 (2000).
26. Troyon, F. et al. MHD-limits to plasma confinement. *Plasma Phys. Control. Fusion* **26**, 209–215 (1984).
27. Fenstermacher, M. E. et al. Effect of island overlap on edge localized mode suppression by resonant magnetic perturbations in DIII-D. *Phys. Plasmas* **15**, 056122 (2008).
28. Park, G., Chang, C. S., Joseph, I. & Moyer, R. A. Plasma transport in stochastic magnetic field caused by vacuum resonant magnetic perturbations at diverted tokamak edge. *Phys. Plasmas* **17**, 102503 (2010).
29. Fitzpatrick, R. Nonlinear error-field penetration in low density ohmically heated tokamak plasmas. *Plasma Phys. Control. Fusion* **54**, 094002 (2012).
30. Waelbroeck, F. L., Joseph, I., Nardon, E., Bécoulet, M. & Fitzpatrick, R. Role of singular layers in the plasma response to resonant magnetic perturbations. *Nucl. Fusion* **52**, 074004 (2012).
31. Callen, J. D., Hegna, C. C. & Cole, A. J. Magnetic-flutter-induced pedestal plasma transport. *Nucl. Fusion* **53**, 113015 (2013).
32. Bécoulet, M. et al. Mechanisms of edge localized mode mitigation by resonant magnetic perturbations. *Phys. Rev. Lett.* **113**, 115001 (2014).
33. Wade, M. R. et al. Advances in the physics understanding of ELM suppression using resonant magnetic perturbations in DIII-D. *Nucl. Fusion* **55**, 023002 (2015).
34. Paz-Soldan, C. et al. Observation of a multimode plasma response and its relationship to density pumpout and edge-localized mode suppression. *Phys. Rev. Lett.* **114**, 105001 (2015).
35. Orain, R. et al. Non-linear modeling of the plasma response to RMPs in ASDEX Upgrade. *Nucl. Fusion* **57**, 022013 (2017).
36. In, Y., Park, J.-K., Jeon, J. M., Kim, J. & Okabayashi, M. Extremely low intrinsic non-axisymmetric field in KSTAR and its implications. *Nucl. Fusion* **55**, 043004 (2015).
37. Park, J.-K., Boozer, A. H. & Glasser, A. H. Computation of three-dimensional tokamak and spherical torus equilibria. *Phys. Plasmas* **14**, 052110 (2007).
38. Callen, J. D. et al. *Model of n = 2 RMP ELM Suppression in DIII-D* Report UW-CPTC 16-4 (University of Wisconsin–Madison Center for Plasma Theory and Computation, 2016); http://www.cptc.wisc.edu
39. Boozer, A. H. Error field amplification and rotation damping in tokamak plasmas. *Phys. Rev. Lett.* **86**, 5059–5061 (2001).
40. Shaing, K. C. & Callen, J. D. Neoclassical flows and transport in nonaxisymmetric toroidal plasmas. *Phys. Fluids* **26**, 3315–3326 (1983).
41. Lanctot, M. J. et al. Validation of the linear ideal magnetohydrodynamic model of three-dimensional tokamak equilibria. *Phys. Plasmas* **17**, 030701 (2010).
42. Wang, Z. R., Lanctot, M. J., Liu, Y. Q., Park, J.-K. & Menard, J. E. Three-dimensional drift kinetic response of high-beta plasmas in the DIII-D tokamak. *Phys. Rev. Lett.* **114**, 145005 (2015).
43. Park, J.-K. & Logan, N. C. Self-consistent perturbed equlibrium with neoclassical toroidal torque in tokamaks. *Phys. Plasmas* **24**, 032505 (2017).
44. Lee, S. G. et al. Validation of toroidal rotation and ion temperature in KSTAR plasmas. *Fusion Sci. Technol.* **69**, 555–559 (2016).
45. In, Y. et al. Enhanced understanding of non-axisymmetric intrinsic and controlled field impacts in tokamaks. *Nucl. Fusion* **57**, 116054 (2017).

Acknowledgements

The authors would like to thank all the KSTAR team members for their support and assistance to our studies. We also wish to acknowledge Alberto Roarte, in the ITER organization, for illuminating discussions of the results and applications. This work was supported by DOE contract DE-AC02-76CH03073 (PPPL) and also by the Korean Ministry of Science and Technology for the KSTAR project.

Author contributions

J.-K.P. carried out the 3D simulations and led the experimental validations. Y.M.J., Y.I., J.-W.A., G.Y.P. and J.K. participated in all the experimental procedures from the initial design to the final execution. R.N. and N.C.L. contributed to the clarification of the issues and the presentation of the results. H.H.L., W.H.K. and H.-S.K. provided reconstructed profiles and plasma equilibria in experiments. Z.W. carried out MARS calculations for benchmark, and E.A.F. visualized the 3D MHD-free window in the coil configuration space. J.E.M. and M.C.Z. offered general guidance to the research.

Competing interests

The authors declare no competing interests.

Additional information

Reprints and permissions information is available at www.nature.com/reprints.

Correspondence and requests for materials should be addressed to J.-K.P.

Publisher's note: Springer Nature remains neutral with regard to jurisdictional claims in published maps and institutional affiliations.

Methods

Choice of rational surfaces for core and edge. The choice of relevant rational surfaces for the core and edge RMP strength depends on the location of rational surfaces relative to the equilibrium profiles. Our hypothesis is that the perturbation to the rational surfaces near or at the top of the steep ∇p pedestal region is important for ELM control, and the perturbation in the core region far from the top of the pedestal is important for LM control. Considering that the top of the pedestal in the studied KSTAR H-mode plasmas is typically located near $\psi_N = 0.95$–0.96, the rational surfaces within $0.93 < \psi_N < 0.98$ are chosen to evaluate the edge RMP Φ_E, whereas the rational surfaces far enough from the edge pedestal, specifically within $\psi_N < 0.8$, are chosen for the core RMP Φ_C. For the $n=1$ applications to $q_{95} = 5.0$–5.2 plasmas discussed in Figs. 1 and 3–5, each RMP is therefore determined by $\Phi_E \equiv \sqrt{|\Phi_{51}|_o^2 + |\Phi_{61}|_o^2}/\sqrt{2}$ and $\Phi_C \equiv \sqrt{|\Phi_{21}|_o^2 + |\Phi_{31}|_o^2}/\sqrt{2}$. More rational surfaces are involved for higher-n applications. The various cases shown in Fig. 6 used (a) $q = m/n = 10/2$, 11/2, 12/2 and $q = 3/2$, 4/2, 5/2, 6/2, (b) $q = 8/2$, 9/2, 10/2 and $q = 4/2$, 5/2, (c) $q = 7/2$, 8/2 and $q = 3/2$, 4/2, 5/2, (d,e) $q = 7/2$, 8/2 and $q = 3/2$, 4/2 and (f) $q = 6/2$ and $q = 3/2$, 4/2 for Φ_E and Φ_C, respectively.

The estimation of $\Phi_{C,E}$ across the multiple rational surfaces reduces sensitivity to the possible errors associated with the equilibrium reconstruction due to the limited capabilities of the deep core and edge profile diagnostics, and also the uncertainties in each penetration process mechanism, in particular the existence and location of a pivotal rational surface. Many EF experiments suggest that the $n=1$ LM-driven disruption occurs due to the resonant field at the $q=2/1$ surface, but no such universal conclusion has been offered for higher-n LMs or ELM suppression. The ability to predict the rational surfaces involved in the bifurcation process will be important to improve $\Phi_{C,E}$ predictions, and also possibly to understand the fine-scale q windows that are often observed[8]. Nevertheless, the phase-space diagrams presented in Figs. 3,4,6 are not particularly sensitive to the small changes in the selected rational surfaces. The window structure is largely determined by global plasma response for the core and edge, as verified by IPEC and also by another 3D MHD code, MARS[46], used as a modelling benchmark.

Determination of critical RMP thresholds. The $n=1$, 2 RMP thresholds for ELM suppression and LM disruption are determined in this work using a single empirical operating point in each case. In the units of Gauss, $(\Phi_E)_{crit} = \Phi_E(I = I_M = 1.8\,\text{kA}, \phi = 90°) \sim 16.3\,\text{G}$ and $(\Phi_C)_{crit} = \Phi_C(I = I_M = 2.1\,\text{kA}, \phi = 90°) \sim 10.0\,\text{G}$ for $n=1$, and $(\Phi_E)_{crit} = \Phi_E(I = I_M = 3\,\text{kA}, \phi = 90°, t = 5.85\,\text{s}) \sim 8.2\,\text{G}$ and $(\Phi_C)_{crit} = \Phi_C(I = I_M = 3\,\text{kA}, \phi = 90°, t = 6.5\,\text{s}) \sim 7.6\,\text{G}$ for $n=2$. These critical RMP values can vary significantly if the dominant kinetic parameters are changed. As empirically found and also theoretically supported, $(\Phi_C)_{crit} \sim n_e^{\alpha_n} B_T^{\alpha_B} R_0^{\alpha_R}$ [29], where the power scaling becomes, for example, $\alpha_n \sim 1.1$, $\alpha_B \sim -1.4$, $\alpha_R \sim -0.6$ across multiple devices if no external toroidal torque is injected[47]. This criterion for $(\Phi_C)_{crit}$ is being used for ITER but is not yet appropriate here for KSTAR due to strong torque from NBI. Nonetheless, the n_e, B_T, R_0, toroidal torque or rotation parameters were not notably varied in the studied experiments even if pressure or q profiles were changed. It is thus a reasonable assumption that $(\Phi_C)_{crit}$ remains almost constant. The same assumption was adopted for $(\Phi_E)_{crit}$, although the parametric dependence of $(\Phi_E)_{crit}$ may be more complicated than that of $(\Phi_C)_{crit}$ due to rapid profile changes in the pedestal, competing transport channels across the 3D field structure and the relatively poor understanding of the physical mechanism impacting ELMs and their crashes. Recently proposed theories[31,46], non-linear MHD simulations[35,49] and advanced diagnostics[13,50] are illuminating, but should be further verified and validated.

The critical RMP values are here estimated based on $\Phi_{C,E} \equiv \left(\sum |\Phi_{mn}|_o^2/N\right)^{1/2}$ and therefore depend on the n values. There is another useful representation for the core and edge RMP strength, called resonant overlap field[51]. This is the first coefficient in the decomposition of external fields on a toroidal control surface using the singular value decomposition vector bases of the coupling matrix $\vec{C}$, between the external 3D fields and the selected $(\Phi_{mn})_o$. When the consistent choices of the rational surfaces are made, $0.93 < \psi_N < 0.98$ for the edge and $\psi_N < 0.8$ for the core, the resonant overlap field yields nearly identical predictions and phase-space diagrams as shown in Figs. 3–6. An advantage of the resonant overlap field is the robust feature in the shape of the first singular value decomposition mode[4,5,52] across tokamak regimes, and this criterion has been adopted for the ITER $n=1$ EF control strategy. Recent EF studies have also implied that it may be possible to develop a single $(\Phi_C)_{crit}$ across $n=1,2$ using the resonant overlap field[53]. Indeed, the method yields similar critical RMP values between $n=1$ and $n=2$: $(\Phi_{oE})_{crit} = \Phi_{oE}(I = I_M = 1.8\,\text{kA}, \phi = 90°) \sim 8.4\,\text{G}$ and $(\Phi_{oC})_{crit} = \Phi_{oC}(I = I_M = 2.1\,\text{kA}, \phi = 90°) \sim 8.9\,\text{G}$ for $n=1$, and $(\Phi_{oE})_{crit} = \Phi_{oE}(I = I_M = 3\,\text{kA}, \phi = 90°, t = 5.85\,\text{s}) \sim 8.6\,\text{G}$ and $(\Phi_{oC})_{crit} = \Phi_{oC}(I = I_M = 3\,\text{kA}, \phi = 90°, t = 6.5\,\text{s}) \sim 7.8\,\text{G}$ for $n=2$, where the extra o subscripts indicate the resonant overlap field bases. That is, the $n=1$ $(\Phi_{oC,oE})_{crit}$ could be used for $n=2$ instead of using the separate $n=2$ operating point. The errors are only about 10–15% and the topological structure of the phase-space diagram shown in Fig. 6 is not sensitive to this level of deviation.

Data availability. The data discussed and used for Figs. 1–6 in this article are available from the corresponding author upon reasonable request.

References

46. Liu, Y., Chu, M. S., Chapman, I. T. & Hender, T. C. Toroidal self-consistent modeling of drift kinetic effects on the resistive wall mode. *Phys. Plasmas* **15**, 112503 (2008).
47. Gribov, Y. et al. Error fields expected in ITER and their correction. In *Proc. 24th IAEA Fusion Energy Conference* ITR/P5–29 (IAEA, Vienna, 2012).
48. Liu, Y. et al. Comparative investigation of ELM control based on toroidal modelling of plasma response to RMP fields. *Phys. Plasmas* **24**, 056111 (2017).
49. Waltz, R. E. & Ferraro, N. M. Theory and simulation of quasilinear transport from external magnetic field perturbations in a DIII-D plasma. *Phys. Plasmas* **22**, 042507 (2015).
50. Lee, J. et al. Nonlinear interaction of edge-localized modes and turbulent eddies in toroidal plasma under $n=1$ magnetic perturbation. *Phys. Rev. Lett.* **117**, 075001 (2016).
51. Park, J.-K., Schaffer, M. J., Haye, R. J. La, Scoville, T. J. & Menard, J. E. Error field correction in DIII-D ohmic plasmas with either handedness. *Nucl. Fusion* **51**, 023003 (2011).
52. Park, J.-K., Schaffer, M. J., La Haye, R. J., Scoville, T. J. & Menard, J. E. Corrigendum: Error field correction in DIII-D ohmic plasmas with either handedness. *Nucl. Fusion* **52**, 089501 (2012).
53. Lanctot, M. J. et al. Impact of toroidal and poloidal mode spectra on the control of non-axisymmetric fields in tokamaks. *Phys. Plasmas* **24**, 056117 (2017).